Audio Engineering Society

Convention Paper 9732

Presented at the 142nd Convention
2017 May 20–23, Berlin, Germany

Further Investigations on the Design of Radial Filters for the Driving Functions of Near-Field Compensated Higher-Order Ambisonics

Nara Hahn and Sascha Spors

Institute of Communications Engineering, University of Rostock, Germany

Correspondence should be addressed to Nara Hahn (nara.hahn@uni-rostock.de)

ABSTRACT

Analytic driving functions for Near-field Compensated Higher-order Ambisonics (NFC-HOA) are derived based on the spherical harmonics expansions of the desired sound field and the Green's function that models the secondary sources. In the frequency domain, the radial part of the driving function is given by spherical Hankel functions compensating the near-field effect of the secondary sources. By exploiting the polynomial expansion of the spherical Hankel functions, the radial filters can be implemented as cascaded biquad filters in the time domain, thereby reducing the computational complexity significantly. In this paper, three practical issues regarding the design of the radial filters are addressed: pole-zero computation, pole-zero mapping, and gain normalization. Improvements in terms of stability and numerical accuracy are demonstrated by numerical simulations.

1 Introduction

Near-field compensated higher-order Ambisonics (NFC-HOA) [1, 2] is a well established sound field synthesis technique along with Wave Field Synthesis (WFS) [3, 4]. The aim of these methods is to recreate a desired sound field within a target region by using a loudspeaker array. The individual loudspeakers, called secondary sources, are driven in such a way that the superimposed sound fields match the target sound field.

NFC-HOA is based on the spherical harmonics expansion of the desired (either captured or modelled) sound field, and the driving functions are also represented with a spherical harmonics expansion. The corresponding expansion coefficients include radial filters which perform the range extrapolation of the sound field between the source radius and the array radius [1]. Motivated by the work of [5], the radial filters for NFC-HOA were realized as biquad (second-order section structure) filters in [6] thereby enabling an efficient implementation in the time-domain. The approach exploits an explicit series expansion of the spherical Hankel functions, which is given as the reverse Bessel polynomial. The poles and zeros of a radial filter

are obtained by scaling the roots of the reverse Bessel polynomial of the respective degree. After transforming the poles and zeros from the Laplace domain into the z-domain, digital biquad filters are composed.

Although the theory of radial filters is well understood, some practical issues arise for radial filters of higher orders. As discussed recently in [7], general-purpose root-finding algorithms often fail to find the true roots of the reverse Bessel polynomial, leading to inaccurate and unstable radial filters. In this paper, this is tackled by using the *Aberth-Ehrlich* method with appropriate initial values (Sec. 3.1). The effects of the choice of pole-zero mapping are examined by comparing the bilinear transform and the matched-z transform (Sec. 3.2). It is also pointed out that a proper normalization of the biquad filters is crucial to achieve the desired magnitude response in the frequency domain (Sec. 3.3). The improvements accomplished by the proposed approach are demonstrated by numerical simulations (Sec. 4).

Nomenclature Throughout this paper, the following notational conventions are used. A sound field in the time-frequency domain is denoted by uppercase $S(\mathbf{x}, \omega)$, where the position vector is denoted by $\mathbf{x}$. The angular frequency ω is defined as $\omega = 2\pi f$ with f being the time-frequency. The imaginary unit is denoted by i. The spherical coordinate representation (r, θ, ϕ) is related to the Cartesian coordinate representation by

$$\begin{aligned} x &= r \cos\phi \sin\theta \\ y &= r \sin\phi \sin\theta \\ z &= r \cos\theta \end{aligned}$$

where θ and ϕ denote the colatitude and azimuth angles, respectively.

Spherical harmonics expansion A homogeneous sound field can be expanded by spherical harmonics with respect to the origin of the coordinate system [8, Eq. (6.140)],

$$S(\mathbf{x}, \omega) = \sum_{n=0}^{\infty} \sum_{m=-n}^{n} \breve{S}_n^m(\omega) j_n(\tfrac{\omega}{c} r) Y_n^m(\theta, \phi), \quad (1)$$

where $\breve{S}_n^m(\omega)$ denote the expansion coefficients and $j_n(\cdot)$ the spherical Bessel function of the first kind of order n. The spherical harmonic $Y_n^m(\phi, \theta)$ is defined as

$$Y_n^m(\theta, \phi) = \sqrt{\tfrac{2n+1}{4\pi} \tfrac{(n-m)!}{(n+m)!}} P_n^m(\cos\theta) e^{im\phi}, \quad (2)$$

where $P_n^m(\cdot)$ denotes the associated Legendre polynomial. The expansion coefficient of a plane wave is given as

$$\breve{S}_{n,\mathrm{pw}}^m(\omega) = 4\pi i^{-n} Y_n^{m*}(\theta_{\mathrm{pw}}, \phi_{\mathrm{pw}}), \quad (3)$$

where $(\theta_{\mathrm{pw}}, \phi_{\mathrm{pw}})$ defines the propagation direction. The asterisk $(\cdot)^*$ denotes the complex conjugate. The expansion coefficient of a point source reads

$$\breve{S}_{n,\mathrm{ps}}^m(\omega) = -i \tfrac{\omega}{c} h_n^{(2)}(\tfrac{\omega}{c} r_{\mathrm{ps}}) Y_n^{m*}(\theta_{\mathrm{ps}}, \phi_{\mathrm{ps}}), \quad (4)$$

where $(r_{\mathrm{ps}}, \theta_{\mathrm{ps}}, \phi_{\mathrm{ps}})$ defines the source position in the spherical coordinate system. $h_n^{(2)}(\cdot)$ denotes the spherical Hankel function of the second kind of order n.

2 NFC-HOA

The problem of sound field synthesis is formulated by the synthesis equation,

$$S(\mathbf{x}, \omega) = \int_{\partial\Omega_0} D(\mathbf{x}_0, \omega) G(\mathbf{x} - \mathbf{x}_0, \omega) \mathrm{d}A(\mathbf{x}_0) \quad (5)$$

for $^\forall\mathbf{x} \in \Omega_0$, where the desired sound field $S(\mathbf{x}, \omega)$ is recreated as a superposition of the individual sound fields emitted by the secondary sources. The secondary sources are distributed on the boundary of the target region $\mathbf{x}_0 \in \partial\Omega_0$. The surface element is denoted by $\mathrm{d}A(\mathbf{x}_0)$. The integral equation has to be solved with respect to the driving function $D(\mathbf{x}_0, \omega)$ for all $\mathbf{x}$ within the target region Ω_0. The Green's function $G(\mathbf{x} - \mathbf{x}_0, \omega)$ describes the spatio-temporal transfer function of each secondary source.

Since NFC-HOA considers only spherical and circular distributions of secondary sources, (5) constitutes a spatial convolution of $D(\mathbf{x}, \omega)$ and $G(\mathbf{x}, \omega)$ on a sphere or a circle. The NFC-HOA driving functions are derived in the spherical/circular harmonics domain, where the spatial convolution is converted to a multiplication [9]. For spherical distributions of secondary point sources, the NFC-HOA driving functions are derived in the spherical

harmonics domain and referred to as 3D NFC-HOA driving functions. For circular distributions of secondary line sources, 2D NFC-HOA driving functions are obtained in the circular harmonics domain. Although not fulfilling the theoretical requirements for sound field synthesis, circular distributions of secondary point sources are often considered in practical systems. Such a configuration is termed 2.5D due to the dimensionality mismatch between the desired sound field (2D) and the secondary source type (3D). Secondary point sources can be realized reasonably well by currently available loudspeakers at lower frequencies. In thie paper, 3D and 2.5D NFC-HOA are considered.

In the following, the 3D and 2.5D driving functions for virtual plane waves and point sources are briefly introduced. For detailed derivations, the readers are referred to [10, Sec. 3.3 and 3.5].

2.1 3D Driving Functions

The 3D NFC-HOA driving function reads [10, Sec. 3.3.1]

$$D_{\mathrm{3D}}(\mathbf{x}_0,\omega) = \sum_{n=0}^{\infty}\sum_{m=-n}^{n} \underbrace{\frac{1}{r_0^2}\sqrt{\frac{2n+1}{4\pi}}\frac{\breve{S}_n^m(\omega)}{\breve{G}_n^0(\omega)}}_{\breve{D}_n^m(r_0,\omega)} Y_n^m(\theta_0,\phi_0) \tag{6}$$

where the properties of the spatial convolution on a spherical surface are exploited [9, (82)]. The secondary source position is represented in the spherical coordinate system, $\mathbf{x}_0 = (r_0, \theta_0, \phi_0)$. The coefficient of the Green's function is defined for the secondary point source at $\theta_0 = 0$ and $\phi_0 = 0$,

$$\breve{G}_n^0(\omega) = -i\tfrac{\omega}{c} h_n^{(2)}(\tfrac{\omega}{c} r_0) \underbrace{Y_n^{0*}(0,0)}_{=\sqrt{\frac{2n+1}{4\pi}}}. \tag{7}$$

Note that only the 0-th order of $\breve{G}_n^m$ is needed.

For a virtual plane wave, the expansion coefficient of the 3D driving function is obtained by plugging (3) and (7) into (6),

$$\breve{D}_{n,\mathrm{pw}}^m(r_0,\omega) = \frac{1}{r_0^2}\underbrace{\frac{4\pi i^{-n}}{-i\frac{\omega}{c}h_n^{(2)}(\frac{\omega}{c}r_0)}}_{H_{n,\mathrm{pw}}(\omega)} Y_n^{m*}(\theta_{\mathrm{pw}},\phi_{\mathrm{pw}}). \tag{8}$$

The 3D driving function for a virtual point source is obtained by plugging (4) and (7) into (6),

$$\breve{D}_{n,\mathrm{ps}}^m(\omega) \tag{9}$$

$$= \frac{1}{r_0^2}\underbrace{\frac{h_n^{(2)}(\frac{\omega}{c}r_{\mathrm{ps}})}{h_n^{(2)}(\frac{\omega}{c}r_0)}}_{H_{n,\mathrm{ps}}(\omega)} Y_n^{m*}(\theta_{\mathrm{ps}},\phi_{\mathrm{ps}}). \tag{10}$$

The underbraced terms in (8) and (10), denoted by $H_{n,\mathrm{pw}}(\omega)$ and $H_{n,\mathrm{ps}}(\omega)$ respectively, constitute the radial parts of the driving functions.

2.2 2.5D Driving Functions

The 2.5D NFC-HOA driving function is represented as a circular harmonics expansion [10, Sec. 3.5.1]

$$D_{\mathrm{2.5D}}(\mathbf{x}_0,\omega) = \sum_{m=-\infty}^{\infty} \underbrace{\frac{1}{2\pi r_0}\frac{\breve{S}_{|m|}^m(\omega)}{\breve{G}_{|m|}^m(\omega)}}_{\mathring{D}_m(r_0,\omega)} e^{im\phi_0}, \tag{11}$$

where $\mathring{D}_m(r_0,\omega)$ denotes the expansion coefficient. Note that only a subset of the coefficients of $\breve{S}_n^m(\omega)$ and $\breve{G}_n^m(\omega)$ are used, i.e. $n = |m|$. Here, the coefficients of the Green's function are defined for the secondary point source at $\theta_0 = \pi/2, \phi_0 = 0$,

$$\breve{G}_{|m|}^m(\omega) = -i\tfrac{\omega}{c} h_{|m|}^{(2)}(\tfrac{\omega}{c} r_0) Y_{|m|}^{m*}(\tfrac{\pi}{2}, 0). \tag{12}$$

The driving functions for virtual plane waves and point sources can be obtained by substituting (3), (4) and (12) into (11),

$$\mathring{D}_{m,\mathrm{pw}}(\omega) = \frac{1}{2\pi r_0}\underbrace{\frac{4\pi i^{-|m|}}{-i\frac{\omega}{c}h_{|m|}^{(2)}(\frac{\omega}{c}r_0)}}_{H_{m,\mathrm{pw}}(\omega)} e^{-im\phi_{\mathrm{pw}}} \tag{13}$$

and

$$\mathring{D}_{m,\mathrm{ps}}(\omega) = \frac{1}{2\pi r_0}\underbrace{\frac{h_{|m|}^{(2)}(\frac{\omega}{c}r_{\mathrm{ps}})}{h_{|m|}^{(2)}(\frac{\omega}{c}r_0)}}_{H_{m,\mathrm{ps}}(\omega)} e^{-im\phi_{\mathrm{ps}}}, \tag{14}$$

respectively.

Note that the radial parts (underbraced) in (13) and (14) are identical to the radial parts of the 3D NFC-HOA driving functions, (8) and (10), respectively.

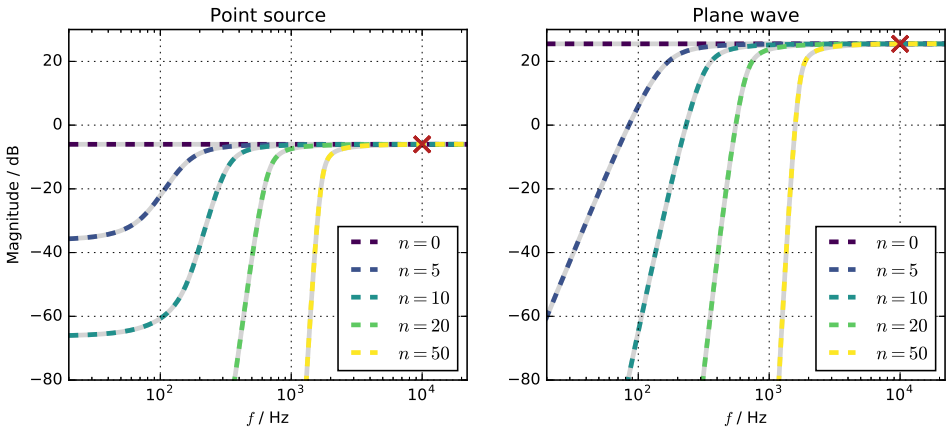

Fig. 1: Magnitude responses of the radial filters for virtual point sources (left) and virtual plane waves (right) for different orders n. The gray lines —— indicate the responses computed directly from the spherical Hankel functions, (10) and (8), while the dashed lines **- - -** are computed from the polynomial expansion (20) and (21). The red cross ✕ indicates the gain at the passband of each radial filter, $\frac{r_0}{r_{\mathrm{ps}}}$ for the point source and $4\pi r_0$ for the plane wave. The radius of the secondary source distribution is $r_0 = 1.5$ m, and the source radius is $r_{\mathrm{ps}} = 3$ m.

3 Radial Filter Design

The radial part of the NFC-HOA driving functions are realized by a digital filter, termed radial filter. The corresponding frequency response depends on the radius of the array r_0 and on the source radius r_{ps} (for virtual point sources). In Fig. 1, the magnitude responses of radial filters are shown for different virtual source types and different orders n. The radial filters are low-frequency shelving filters for virtual point sources and high-pass filters for virtual plane waves. The cut-off frequency increases with the filter order. For a given virtual source, the gain at the passband (indicated by red crosses) is constant,

$$|H_{n,\mathrm{pw}}(\omega)|_{\omega\to\infty} = \frac{r_0}{r_{\mathrm{ps}}} \tag{15}$$

$$|H_{n,\mathrm{ps}}(\omega)|_{\omega\to\infty} = 4\pi r_0. \tag{16}$$

independent to the order n. As shown in Fig. 2, the gain in inversely proportional to the source distance r_{ps} (left) and proportional to the radius of the secondary source distribution r_0 (right).

Due to the spherical Hankel functions, a direct implementation of the radial filters in the frequency domain is computationally demanding. In [5, Sec. 3.5.3], an efficient implementation was introduced where the radial filters were realized as digital biquad filters, i.e. first- and second-order section structures [11, Sec. 6.3.2]. The filter design process is as follows:

1. The roots of the reverse Bessel polynomial are numerically computed and the poles and zeros of the radial filters are obtained by scaling the roots.
2. The poles and zeros in the Laplace domain are transformed to the z-domain by using a pole-zero mapping.
3. Digital biquad filters are composed by grouping the z-domain poles and zeros.

In the remainder of this section, each step is described in detail. Some useful suggestions are given for improved stability and numerical accuracy.

3.1 Pole-zero Computation

As a first step, the spherical Hankel function is represented as a series expansion [12, Eq. (10.1.17)]

$$h_n^{(2)}(s) = -i^n e^{-s} \frac{\sum_{k=0}^{n} \beta_n(k) s^k}{s^{n+1}} \tag{17}$$

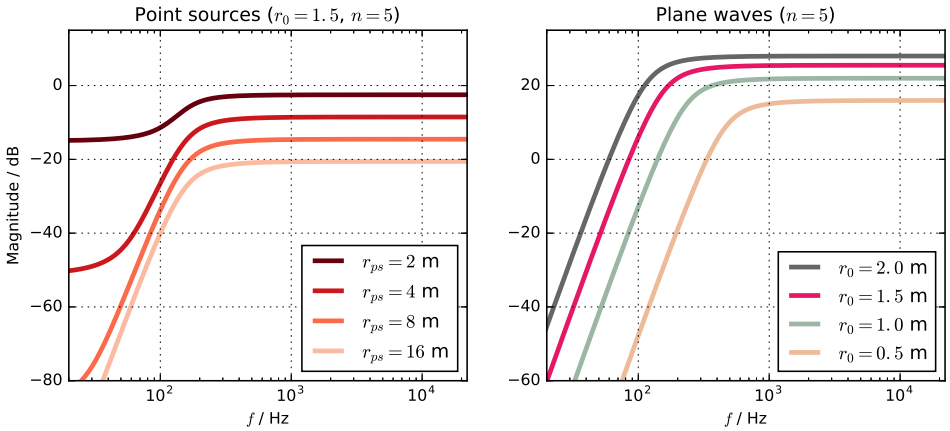

Fig. 2: Magnitude responses of the radial filters for virtual point sources (left) and virtual plane waves (right). For a given filter order n, the passband gain and the stopband gain depend on the source distance r_{ps} while the cut-off frequency is constant. The radius of the array r_0 affects the passband gain as well as the cut-off frequency (right).

where the expansion coefficient $\beta_n(k)$ is given as

$$\beta_n(k) = \frac{(2n-k)!}{(n-k)!k!2^{n-k}}. \tag{18}$$

Equation (17) is known as the reverse Bessel polynomial of degree n. By using complex conjugate roots $\sigma_l \pm i\omega_l$ of the polynomial, the spherical Hankel function can be represented as a factored polynomial,

$$h_n^{(2)}(s) = -i^n e^{-s} \times (s-\sigma_0)^{\mu} \frac{\prod_{l=1}^{\nu}(s-\sigma_l)^2 + \omega_l^2}{s^{n+1}} \tag{19}$$

where $\nu = \mathrm{div}(n,2)$ and $\mu = \mathrm{mod}(n,2)$. For odd n, the first root is real-valued, i.e. $s_0 = \sigma_0$.

By exploiting (19), the radial filters for a virtual point source can be represented as a cascade of first- and second-order section filters [6, Eq. (11)],

$$H_{n,\mathrm{ps}}(s) = \frac{r_0}{r_{\mathrm{ps}}} e^{-\frac{s}{c}(r_{\mathrm{ps}}-r_0)} \times \left(\frac{s-\frac{c}{r_{\mathrm{ps}}}\sigma_0}{s-\frac{c}{r_0}\sigma_0}\right)^{\mu} \prod_{l=1}^{\nu} \frac{\left(s-\frac{c}{r_{\mathrm{ps}}}\sigma_l\right)^2 + \left(\frac{c}{r_{\mathrm{ps}}}\omega_l\right)^2}{\left(s-\frac{c}{r_0}\sigma_l\right)^2 + \left(\frac{c}{r_0}\omega_l\right)^2} \tag{20}$$

where the poles and zeros are obtained by scaling the roots of the reverse Bessel polynomial by $\frac{c}{r_{\mathrm{ps}}}$ and $\frac{c}{r_0}$ respectively. Similarly, the radial filter for a virtual plane wave reads [6, (10)]

$$H_{n,\mathrm{pw}}(s) = 4\pi r_0 (-1)^n e^{\frac{s}{c}r_0} \times \left(\frac{s}{s-\frac{c}{r_0}\sigma_0}\right)^{\mu} \prod_{l=1}^{\nu} \frac{s^2}{\left(s-\frac{c}{r_0}\sigma_l\right)^2 + \left(\frac{c}{r_0}\omega_l\right)^2} \tag{21}$$

where the poles are obtained by scaling the roots by $\frac{c}{r_0}$. The zeros are at $s = 0$.

Since the zeros and poles of the radial filters are determined by the roots of the reverse Bessel polynomials, it is crucial to compute the roots accurately. However, exact algebraic roots are not known for the polynomial. The roots can be obtained only by numerical methods. The most commonly used root finding algorithm is based on the companion matrix of the polynomial [13, Sec. 7.4.6]. The roots are obtained by computing the eigenvalues of the companion matrix. The method is implemented in Matlab (`roots`) and Python (`numpy.roots`).

Unfortunately, the algorithm is not suited for reverse Bessel polynomials, in particular for higher degrees. It was shown in [14] that the real and imaginary part of the roots can be approximated by cubic and quadratic functions. However, the roots computed by the companion matrix method deviate from the expected locations in the complex plane. This is shown in Fig. 3 for different

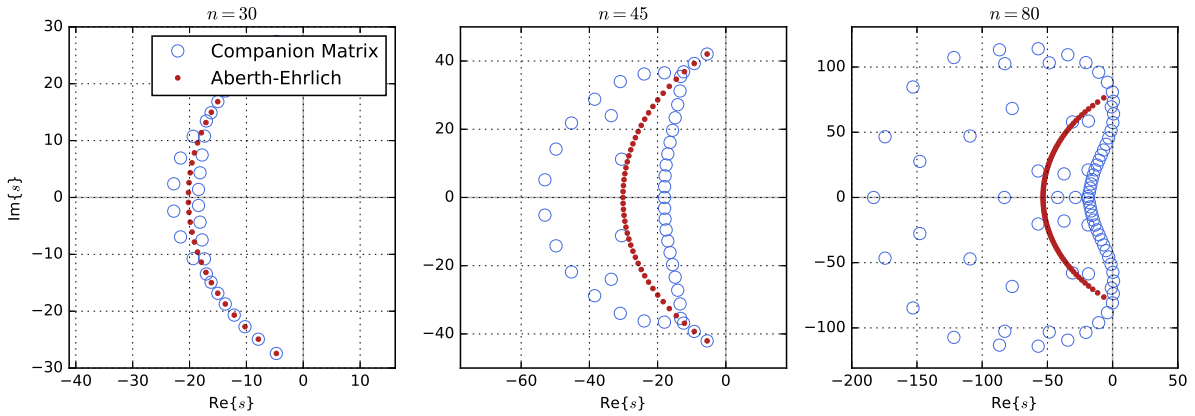

Fig. 3: Roots of the reverse Bessel polynomials of different degrees $n = 30, 45, 80$. The roots computed with the companion matrix method are indicated by blue circles ◯ whereas the roots computed with the Abert-Ehrlich method are indicated by red dots •. Note the different ranges of the axes.

degrees. The deviation is more severe in higher degrees. For $n = 80$, some of the roots are on the right half plane which will result in an unstable filter. Increasing the numerical precision does not seem to overcome the problem [7].

In this study, the Aberth-Ehrlich method is suggested instead which is an iterative algorithm for a simultaneous computation of the roots of a polynomial [15, 16]. The initial values for the iteration are chosen as the approximate roots proposed in [14]. The resulting roots are shown in Fig. 3. Since the algebraic roots (ground truth) are not known, absolute errors of the roots cannot be evaluated. Still, the improvements over the companion matrix method are apparent, as the roots are placed on a smooth curve as observed in [14]. In this study, a Python implementation of the Aberth-Ehrlich method (`scipy.signal.besselap`) is used. This allows to compute the roots of the reverse Bessel polynomial up to the degree of $m = 150$ using double precision numbers.

The radial filters computed with (20) and (21) are shown in Fig. 1, indicated by dashed lines. The magnitude responses are compared with the radial parts computed with (10) and (8) respectively.

3.2 Pole-zero Mapping

Once the zeros and poles of the radial filters are obtained in the Laplace domain, these have to be transformed into the z-domain in order to implement the filter in the discrete-time domain. In this study, the bilinear transform and the matched-z transform are used and their influences on the radial filter design are compared [17]. Only virtual point sources ($r_{\mathrm{ps}} = 3$ m) are considered.

The frequency responses using two different mappings are compared in Fig. 4. The magnitude and phase errors with respect to the desired response are shown. For both methods, the errors increases with the filter order. In the passband, the difference between the two methods is almost negligible. The matched-z transform exhibits a slightly better performance in the transition band. The difference in the phase responses are marginal except in the transition band.

3.3 Gain Normalization

Finally, the poles and zeros in the z-domain are used to compose first- and second-order section filters. In this stage, the gain of each second-order section filter has to be taken into account. Its importance is twofold. Since the driving functions are obtained by adding up the radial filters, the relative gain has to be maintained. Otherwise spectral distortions will occur. The absolute gain is also of importance in order to obtain a correct amplitude decay for varying source distances. As shown in Fig. 5, the magnitude responses in the

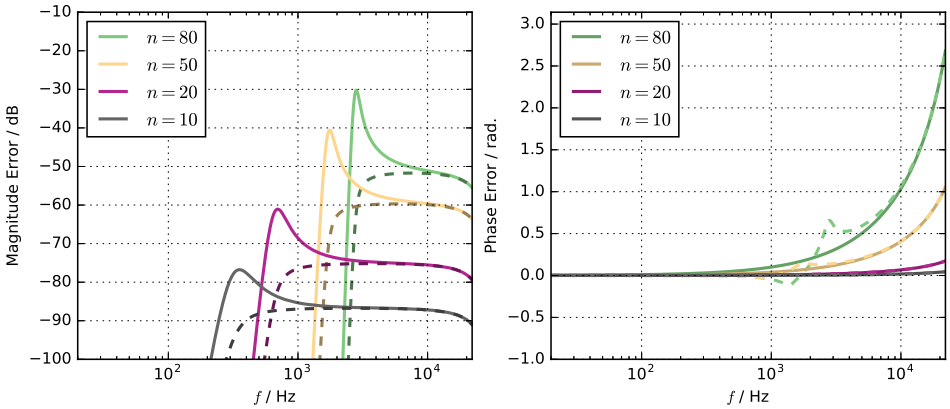

Fig. 4: Frequency response errors of the radial filters for different pole-zero mappings. The solid lines —— indicates the bilinear transform while the dashed line - - - indicates the matched-z transform. The magnitude errors with respect to the desired response are shown in the left, while the phase errors are shown in the right. The radial filters are computed for a virtual point source ($r_{\mathrm{ps}} = 3, r_0 = 1.5$).

passband suffer from unwanted amplification if the gain is not normalized.

The gain should not be normalized to an arbitrarily chosen value, e.g. 0 dB, but to the true value. The magnitude response at $z = -1$ (Nyquist frequency) in the z-domain is matched with the magnitude response at $s = i\pi f_s$ in the Laplace domain. The gain correction term thus reads

$$g_n = \frac{|H_n(s)|_{s=i\pi f_s}}{|H_n(z)|_{z=-1}}. \tag{22}$$

This improved the accuracy of the magnitude responses of the radial filters, as shown in Fig. 5.

3.4 Summary

The discrete-time radial filters read

$$H_{n,\mathrm{ps}}(z) = \frac{r_0}{r_{\mathrm{ps}}} B(z, \tfrac{r_{\mathrm{ps}} - r_0}{c}) \times g_n \left(\frac{z - z_{0,0}}{z - z_{\infty,0}} \right)^{\mu} \prod_{l=0}^{\nu} \frac{(z - z_{0,l})(z - z_{0,l}^*)}{(z - z_{\infty,l})(z - z_{\infty,l}^*)}. \tag{23}$$

for virtual point sources and

$$H_{n,\mathrm{pw}}(z) = 4\pi r_0 (-1)^n B(z, -\tfrac{r_0}{c}) \times g_n \left(\frac{z}{z - z_{\infty,0}} \right)^{\mu} \prod_{l=0}^{\nu} \frac{z^2}{(z - z_{\infty,l})(z - z_{\infty,l}^*)} \tag{24}$$

for virtual plane waves. The complex conjugate pairs $z_{0,l}, z_{0,l}^*$ and $z_{\infty,l}, z_{\infty,l}^*$ denote the z-domain zeros and poles, respectively. $B(z, \tau)$ realizes the time shift of τ either by using integer delay lines or fractional delay filters. The normalization gain g_n is given in (22).

Finally, the discrete-time driving functions are obtained by substituting (23) and (24) into the 3D driving functions (10) and (8) or the 2.5D driving functions (14) and (13). As shown in Table 1, the driving functions can be decomposed into four parts: overall delay, overall gain, order-dependent radial part, and order-dependent angular part. For instance, the 2.5D driving function can be realized as illustrated in Fig. 6.

4 Evaluation

4.1 Modal Impulse Responses

The impulse responses of the radial filters are obtained by filtering an unit impulse function with the cascaded biquad filters. As shown in Fig. 7, the 0-th modal impulse response corresponds to an impulse. As n increases, the modal responses oscillates with higher frequencies which agrees with the high-pass characteristic of the radial filters. The influence of the root finding methods discussed in

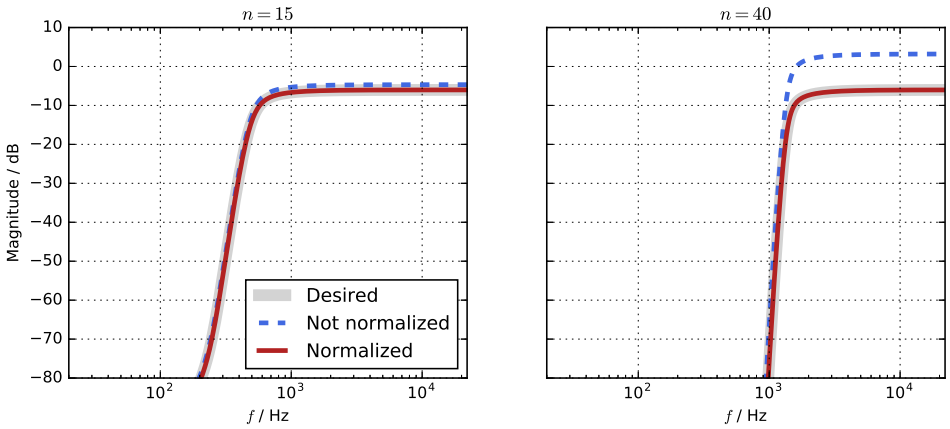

Fig. 5: Magnitude responses of the radial filters with — and without - - - gain normalization. The radial filters ($n = 15, 40$) are computed for a virtual point source with $r_0 = 1.5, r_{\mathrm{ps}} = 3$. The gain is normalized using (22).

Sec. 3.1 is observed for higher orders. Due to the poles in the right half plane in the Laplace domain, or equivalently the poles outside the unit circle in the z domain, the corresponding radial filters suffer from instabilities (indicted by gray lines).

4.2 Synthesized Sound Fields

The driving functions were used to simulate the synthesized sound field by using the Sound Field Synthesis Toolbox [18]. A 2.5D configuration was considered where 60 secondary point sources are equiangularly placed on a circle of radius $r_0 = 1.5$ m. The driving functions for a virtual point source and a virtual plane wave were computed. A unit impulse signal was filtered with the driving functions and reproduced by the individual secondary point sources. Temporal snapshots of the synthesized sound fields are shown in Fig. 8. In the left column, the harmonics expansion in (11) is truncated to the maximum order of $M = 30$ which avoids the overlap of the repeated circular harmonic spectra [10, Sec. 4.4]. The sound field is synthesized almost perfectly at the expansion center (origin) but strong impairments are observed elsewhere. In the right column, the harmonics expansion is truncated to $M = 120$ which causes spectral overlap of the circular harmonic spectra, i.e. spatial aliasing. Compared to the case of $M = 30$, the desired wavefronts are synthesized more accurately throughout the target area. This comes at the cost of the additional waves that follow the main wavefront. If the maximum order is further increased, the synthesized sound field resembles the sound field of WFS. WFS driving functions are computed based on the representation of the sound field with an infinite spatial bandwidth.

5 Conclusion

In this paper, the design of radial filters for NFC-HOA driving functions was revisited. It is shown that the stability and numerical accuracy of the driving functions are affected by the locations of the poles and zeros of the radial filters. A significant improvement can be achieved by using an iterative root finding algorithm, the Aberth-Ehrlich method. This allows to design radial filters of order up to order of 150 without numerical instabilities. Two pole-zero mappings, the bilinear transform and the matched-z transform, were compared but the difference was rather subtle. The importance of normalizing the biquad filters was also discussed.

Acknowledgement

This research has been supported by DFG SP 1295/7-1.

	Weight	Delay	Radial part (biquad filters)	Angular part
3D, ps	$\frac{1}{r_0 r_{\mathrm{ps}}}$	$\frac{r_{\mathrm{ps}}-r_0}{c}$	$g_n \left(\frac{z-z_{0,0}}{z-z_{\infty,0}}\right)^{\mu} \prod_{l=0}^{\nu} \frac{(z-z_{0,l})(z-z_{0,l}^*)}{(z-z_{\infty,l})(z-z_{\infty,l}^*)}$	$Y_n^{m*}(\theta_{\mathrm{ps}}, \phi_{\mathrm{ps}}) Y_n^m(\theta_0, \phi_0)$
3D, pw	$\frac{4\pi}{r_0}$	$\frac{-r_0}{c}$	$g_n \left(\frac{z}{z-z_{\infty,0}}\right)^{\mu} \prod_{l=0}^{\nu} \frac{z^2}{(z-z_{\infty,l})(z-z_{\infty,l}^*)}$	$(-1)^n Y_n^{m*}(\theta_{\mathrm{pw}}, \phi_{\mathrm{pw}}) Y_n^m(\theta_0, \phi_0)$
2.5D, ps	$\frac{1}{2\pi r_{\mathrm{ps}}}$	$\frac{r_{\mathrm{ps}}-r_0}{c}$	$g_m \left(\frac{z-z_{0,0}}{z-z_{\infty,0}}\right)^{\mu} \prod_{l=0}^{\nu} \frac{(z-z_{0,l})(z-z_{0,l}^*)}{(z-z_{\infty,l})(z-z_{\infty,l}^*)}$	$e^{im(\phi_0-\phi_{\mathrm{ps}})}$
2.5D, pw	2	$\frac{-r_0}{c}$	$g_m \left(\frac{z}{z-z_{\infty,0}}\right)^{\mu} \prod_{l=0}^{\nu} \frac{z^2}{(z-z_{\infty,l})(z-z_{\infty,l}^*)}$	$(-1)^m e^{im(\phi_0-\phi_{\mathrm{pw}})}$

Table 1: NFC-HOA driving functions. Each driving function consists of an overall weight, overall delay, order-dependent radial filter, and an order-dependent angular term.

References

[1] Daniel, J., "Spatial Sound Encoding including Near Field Effect: Introducing Distance Coding Filters and a Viable, new Ambisonic Format," in *Proc. of 23rd Audio Engineering Society (AES) International Conference on Signal Processing in Audio Recording and Reproduction*, Helsingør, Denmark, 2003.

[2] Ahrens, J. and Spors, S., "An Analytical Approach to Sound Field Reproduction using Circular and Spherical Loudspeaker Distributions," *Acta Acustica united with Acustica*, 94(6), pp. 988–999, 2008.

[3] Berkhout, A. J., de Vries, D., and Vogel, P., "Acoustic Control by Wave Field Synthesis," *The Journal of the Acoustical Society of America (JASA)*, 93(5), pp. 2764–2778, 1993.

[4] Spors, S., Rabenstein, R., and Ahrens, J., "The theory of Wave Field Synthesis revisited," in *Proc. of 124th Audio Engineering Society (AES) Convention*, 2008.

[5] Pomberger, H., *Angular and Radial Directivity Control for Spherical Loudspeaker Arrays*, Diploma Thesis, Institute of Electronic Music and Acoustics, University of Music and Dramatic Arts, Graz, Austria, 2008.

[6] Spors, S., Kuscher, V., and Ahrens, J., "Efficient Realization of Model-based Rendering for 2.5-dimensional Near-field Compensated Higher Order Ambisonics," in *Proc. of IEEE Workshop on Applications of Signal Processing to Audio and Acoustics (WASPAA)*, New Paltz, USA, 2011.

[7] "Second-order Structure Filters for NFC-HOA Driving Function," `https://github.com/sfstoolbox/sfs-matlab/issues/57`, 2016, accessed: 2016-05-01.

[8] Williams, E. G., *Fourier Acoustics: Sound Radiation and Nearfield Acoustical Holography*, Academic press, 1999.

[9] Baddour, N., "Operational and Convolution Properties of Three-dimensional Fourier Transforms in Spherical Polar Coordinates," *Journal of the Optical Society of America (JOSA) A*, 27(10), pp. 2144–2155, 2010.

[10] Ahrens, J., *Analytic Methods of Sound Field Synthesis*, Springer, 2012.

[11] Oppenheim, A. V., Schafer, R. W., and Buck, J. R., *Discrete-time Signal Processing*, Prentice Hall, 1999.

[12] Abramowitz, M. and Stegun, I. A., *Handbook of Mathematical Functions: with Formulas, Graphs, and Mathematical Tables*, 55, Courier Corporation, 1964.

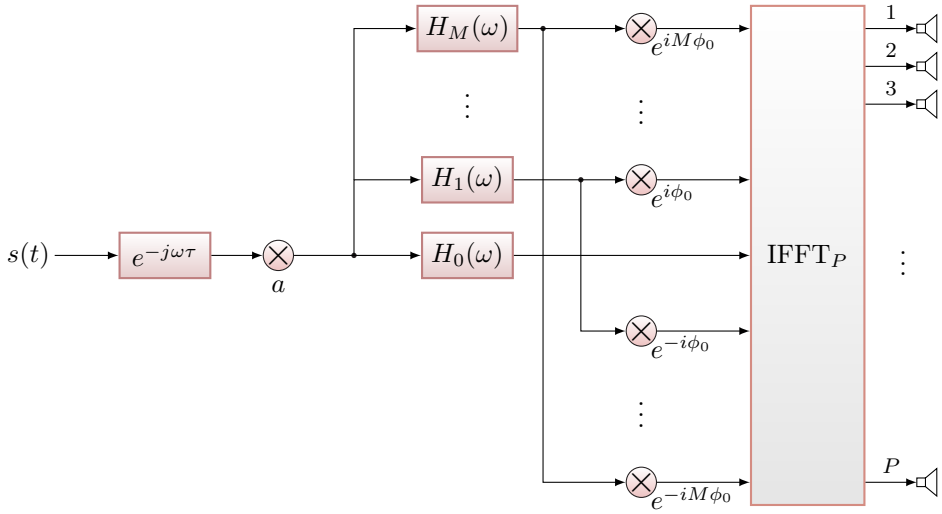

Fig. 6: Block diagram illustrating the implementation of 2.5D NFC-HOA (redrawn from [6, Fig. 2]).

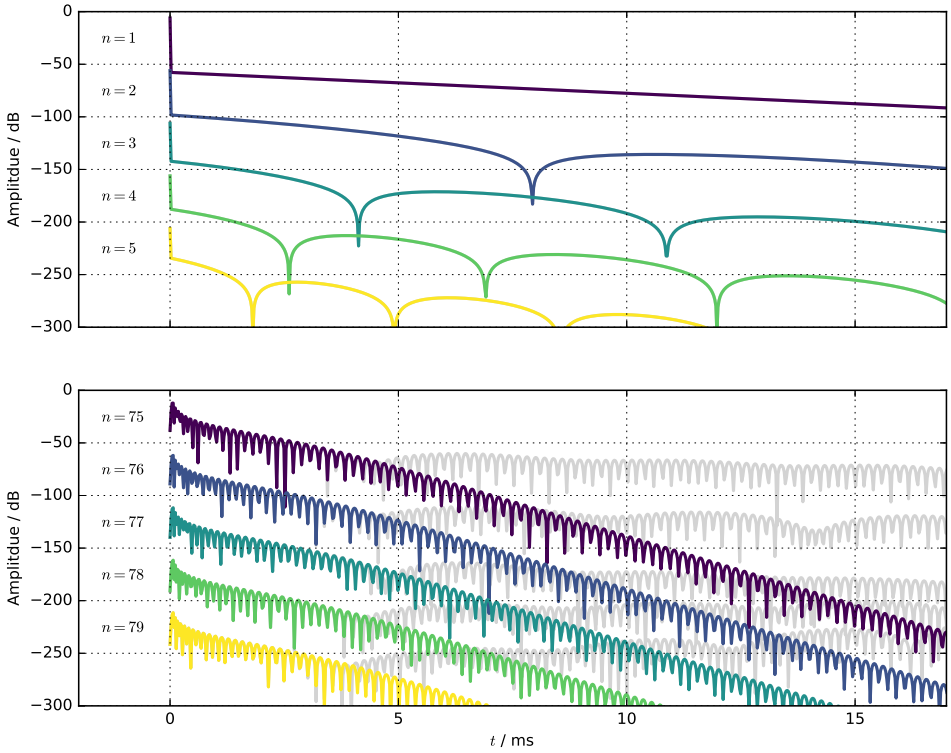

Fig. 7: Impulse responses of the radial filters of different orders. The poles and zeros of the radial filters are computed by using the companion matrix method (indicated by gray lines ——) and the Alberth-Ehrlich method (indicated by colored lines).

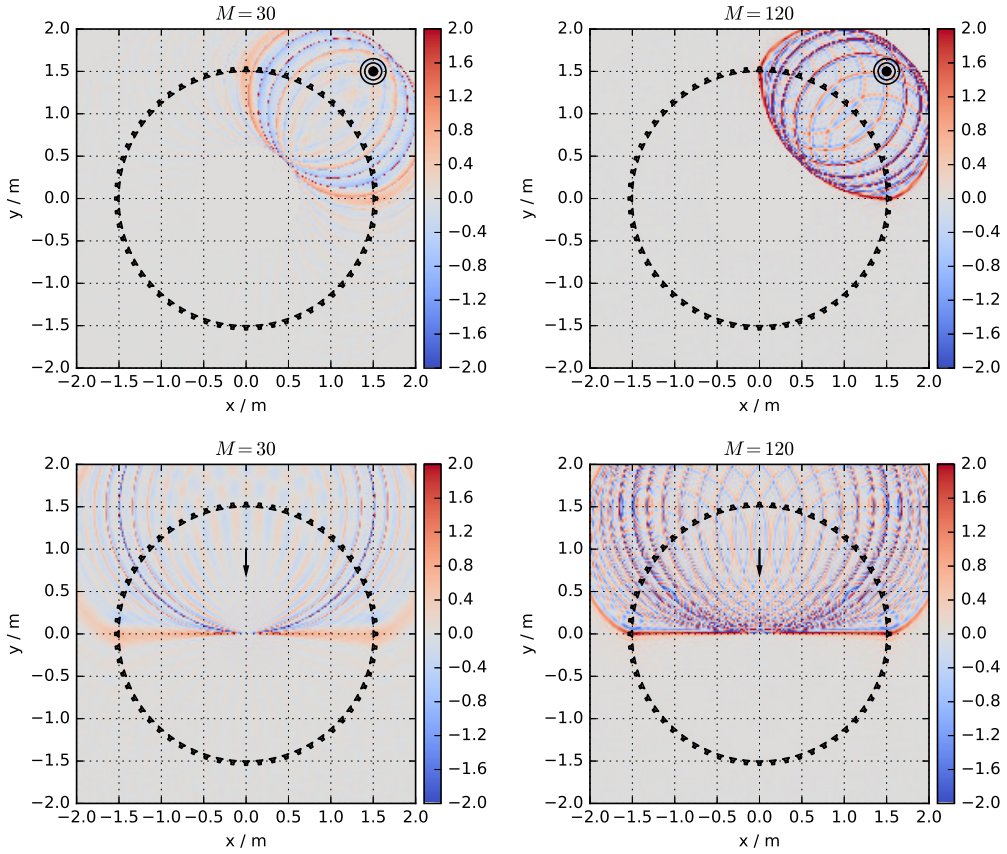

Fig. 8: Synthesized sound field for 2.5D NFC-HOA. Top: Virtual point source at $(1.5, 1.5, 0)$. Bottom: Virtual plane wave propagating with an angle of $\phi = -\frac{\pi}{2}$. 60 secondary sources are equiangularly distributed on a circle of radius $r_0 = 1.5$ m. A unit impulse signal was reproduced. The driving functions are truncated to the maximum order of $M = 30$ (left column) and $M = 120$ (right column).

[13] Golub, G. H. and Van Loan, C. F., *Matrix Computations*, Johns Hopkins University Press, Baltimore, MD,, 1996.

[14] Campos, R. G. and Calderón, M. L., "Approximate Closed-form Formulas for the Zeros of the Bessel Polynomials," *International Journal of Mathematics and Mathematical Sciences*, 2012, 2012.

[15] Aberth, O., "Iteration Methods for Finding All Zeros of a Polynomial Simultaneously," *Mathematics of computation*, 27(122), pp. 339–344, 1973.

[16] Ehrlich, L. W., "A Modified Newton Method for Polynomials," *Communications of the ACM*, 10(2), pp. 107–108, 1967.

[17] Schlichthärle, D., *Digital Filters: Basics and Design*, IOP Publishing, 2001.

[18] Spors, S., Geier, M., and Wierstorf, H., "Sound Field Synthesis Toolbox for Python, Version 0.3.1," 2016, doi:10.5281/zenodo.49356.